



Brooks Range Perennial Snowfields: Extent Detection from the Field and via Satellite

Molly E. Tedesche^{1,2}, Erin D. Trochim³, Steven R. Fassnacht⁴, and Gabriel J. Wolken^{5,6}

¹US Army Corps Engineer Research and Development Center, Cold Regions Research and Engineering Laboratory, Hanover, NH, USA, and Coastal and Hydraulics Laboratory, Vicksburg, MS, USA

²Water and Environmental Research Center, University of Alaska Fairbanks, Fairbanks, AK, USA

³Center for Energy and Power, University of Alaska Fairbanks, Fairbanks, AK, USA

⁴Department of Watershed Science, Colorado State University, Fort Collins, CO, USA

⁵Climate and Cryosphere Hazards Program, Alaska Division of Geological and Geophysical Surveys, Fairbanks, AK, USA

⁶Alaska Climate Adaptation Science Center, University of Alaska Fairbanks, Fairbanks, AK, USA

Correspondence: Molly E. Tedesche (metedesche@alaska.edu)

Abstract. Perennial snowfields are a critical part of the alpine ecosystem, serving as habitat for an array of wildlife species, and influencing downslope hydrology, vegetation, geology, and permafrost. In this study, perennial snowfield extents in the Brooks Range of Arctic Alaska are derived from Synthetic Aperture Radar (SAR) and multi-spectral satellite remote sensing via the Sentinel-1 (S1) and Sentinel-2 (S2) constellations. Snow cover area (SCA) is mapped using multi-spectral analysis in S2 and via the creation of a SAR backscatter change detection algorithm with S1. Results of the remote sensing techniques are evaluated by comparison with field data acquired across multiple spatial resolutions and geographic domains, including helicopter points and manual, on-the-ground collected SCA. Evaluations of the SAR change detection algorithm via comparison with results from multi-spectral imagery analysis, and field acquired data, indicate that the SAR algorithm performs best in small, focused geographic sub-domains. This may be the result of SAR algorithm dependency on thresholding and slope corrections in mountainous terrain. An alternative approach to mapping the perennial snowfields is also presented, as a synthesis of the S1 and S2 results, wherein S1 results are used to fill voids left in the S2 data from cloud masking processes.

1 Introduction

Perennial snowfields, such as those in the Brooks Range Mountains in Alaska, are a critical hydrological component of alpine and arctic ecosystems. They serve as habitat for an array of birds and mammal species (Toupin et al., 1996; Anderson and Nilssen, 1998; Rosvold, 2016), affect subsistence hunting and overland travel for rural people living in the Arctic (Rattenbury et al., 2009), influence soil and bedrock weathering through freeze-thaw cycles (Berrisford, 1991), encourage microbe diversity (Ganey et al., 2017; Hotaling et al., 2019; 2021; Brighenti et al., 2021) and impact hydrology, vegetation (Lewkowicz and Young, 1990), and permafrost distribution (Luetschg et al., 2004). Perennial snowfields, like glaciers, are masses of snow, firn, and ice that persist year-round and form through accumulation and compaction of seasonal snow but are too small to move under the influence of gravity. They are persistent where the climatological snowline intercepts the terrain that limits exposure to solar radiation and is favorable to preferential snow deposition, including wind-influenced snow transport and avalanches



(Lehning et al., 2008; Dadic et al., 2010). These snowfields also occur in regions with less complex topography, such as on plateaus, where persistence is less a product of reduced solar exposure and more a result of drifting and prolonged low air temperature (Wolken et al., 2005). The basis for defining “perennial” is vague for snowfields, as very few have attempted to
25 define a minimum age of persistence to be considered perennial. Among those studies, the minimum number of years to deem a snowfield as perennial range from two (Higuchi et al., 1980; Muller, 1970) to twenty (DeVisser and Fountain, 2015). In 2019, Tedesche et al. considered snowfields as perennial if they persisted year-round for at least four years.

Seasonal and perennial snow and ice cover are monitored using an array of various field-based techniques, as well as with remote sensing via aerial and satellite imagery. A relatively new collection of satellites being used to monitor snow
30 and ice is the Copernicus Sentinel satellite constellation, which consists of multi-spectral imaging from Sentinel-2 (S2) and synthetic aperture radar (SAR) from Sentinel-1 (S1). Often, studies involving automated mapping of snow and ice employ the Normalized Difference Snow Index (NDSI), which uses the green and short-wave infrared spectral bands (Dozier, 1989), in combination with a cloud mask, such as the Fmask algorithm (Zhu and Woodcock, 2012; Zhu et al., 2015). Due to the challenges in discerning clouds from snow in multi-spectral remote sensing, some studies focus on the utility of SAR data
35 via satellite as an alternative for snow detection (Tiuri et al., 1984; Nagler et al., 2016; Lievens et al., 2021). SAR operates independently from cloud cover since radar backscatter, a measure of reflective strength, can be measured through clouds to find snow and ice cover (Mätzler, 1987; Shi and Dozier, 1995; Chang et al., 2014).

SAR change detection algorithms for wet snow (wet snow/firn of perennial snowfields in this study), work on the phenomenon that liquid water dramatically attenuates radar signals (Barker and Watts, 1973) due to high dielectric losses. This
40 reduces the backscatter coefficient (σ^0) of wet snow, compared to dry snow (Evans, 1965; Tiuri et al., 1984). This study takes advantage of these backscatter contrasts to develop a SAR change detection algorithm for finding perennial snowfields in the Brooks Range using S1 SAR C-band data. Refreezing of the snow surface during a cold night can cause an increase in σ^0 due to high scattering characteristics of the frozen layer (Reber et al., 1987; Floricioiu and Rott, 2001). This results in a decrease in the contrast of snow versus snow-free surfaces (Shi and Dozier, 1995; Ulaby et al., 2014), however, data show this effect to
45 be less pronounced with C-band than other bands (Nagler et al., 2016). It is also important to consider incident angular dependence of backscatter, which influences change detection and discernment of perennial snow cover area (SCA). The backscatter contrast between melting snow and snow-free surfaces changes with the local incidence angle of the radar beam return from the ground (Nagler et al., 2016). Employing SAR change detection to map snow across mountainous terrain like the Brooks Range is challenging (Rott and Mätzler, 1987), but not impossible with radiometric terrain corrections (Vollrath et al., 2020).

50 The purpose of this research is to develop a SAR backscatter change detection algorithm for quantifying SCA of perennial snowfields in the Brooks Range, Alaska; and to evaluate the SAR-derived SCA by comparing it with NDSI-derived SCA from multi-spectral imagery and from field observations. To meet this purpose, *five objectives* are addressed in this study: (1) apply NDSI to S2 imagery to quantify perennial snowfield SCA in the Brooks Range; (2) develop an S1 SAR change detection algorithm to quantify SCA in the Brooks Range; (3) compare SCA results from the S1 and S2 analyses with field collected
55 data; (4) compare SCA results between the S1 and S2 analyses; and (5) use S1 and S2 SCA results to map snowfields persisting for at least four years.



2 Study Area

This study compares multiple approaches for quantifying SCA of perennial snowfields in the Brooks Range, Alaska, by utilizing several focused study areas of various extents within the vast expanse of this Arctic mountain range. The Brooks Range covers an immense area where climate varies locally, with extreme seasonal and inter-seasonal temperature ranges, as well as low annual precipitation (Davey et al., 2007; Winfree et al., 2014). These extreme temperature swings are the result of low humidity, nearly continuous daylight during the mid-summer, and very little daylight during mid-winter. Most of the Brooks Range is uninhabited in modern times, as access is limited by lack of roads and extreme terrain. Gates of the Arctic National Park and Preserve (GAAR) is located in the central Brooks Range. Within the park is an Alaska Native withholding where the village of Anaktuvuk Pass (AKP) lies (Elev: 683 m; 68.1433°N, 151.7358°W). The focused study areas for this research are situated around and to the east of AKP (*Figure 1*).

The AKP Study Area covers an area of 5,650 km², wherein results of the remote sensing are compared to helicopter-acquired field data (*Figure 1*) (mean elev: 1,225 m; mean slope: 24°, mean aspect: 177°). The two Local Scale Study Areas, embedded within the AKP mesoscale area, are where remote sensing results are compared to sub-meter scale field data collected on foot in 2016 at East Ingstad Mountain (EIM16; 24 km²; mean elev: 1,310m; mean slope: 29°, mean aspect: 186°) and in 2017 at North Ingstad Mountain (NIM17; 19 km²; mean elev: 1,383 m; mean slope: 29°, mean aspect: 179°) (*Figure 1*). There are only a few small glaciers in GAAR (Evison et al., 1996); anecdotal field work observations indicated that some of these are very small “dead” glaciers no longer growing or moving, or “glacierettes” with characteristics similar to perennial snowfields. Much of the land surface is also covered by aufeis, which accumulates during the winter over rivers and lakes, formed by upwelling of water behind ice dams, by groundwater discharge, and persisting year-round in low-lying valleys with limited exposure to solar radiation (Yoshikawa et al., 2007). Aufeis has a similar spectral signature as perennial snowfields and in this study, it was removed during image pre-processing using elevation thresholds.

3 Data Sources

Sentinel-1 (S1, sentinel.esa.int/web/sentinel/missions/sentinel-1) Synthetic Aperture Radar (SAR) satellite data and Sentinel-2 (S2, sentinel.esa.int/web/sentinel/missions/sentinel-2) multi-spectral (optical) satellite imagery are the primary datasets analyzed to quantify perennial snowfield SCA across the Brooks Range and within several smaller study areas. Green, red, blue, shortwave infrared (SWIR), and near-infrared (NIR) bands from S2 Level-1C Top of Atmosphere (TOA) reflectance are used to calculate NDSI and normalized difference water index (NDWI), as well as for cloud cover detection and masking. S2 imagery from 2016 and 2017 is analyzed to derive perennial snowfield SCA within the AKP mesoscale, EIM16 local scale, and NIM17 local scale study areas. S2 imagery from 2016 through 2019 is then used to map snowfields across the full extent of the Brooks Range.

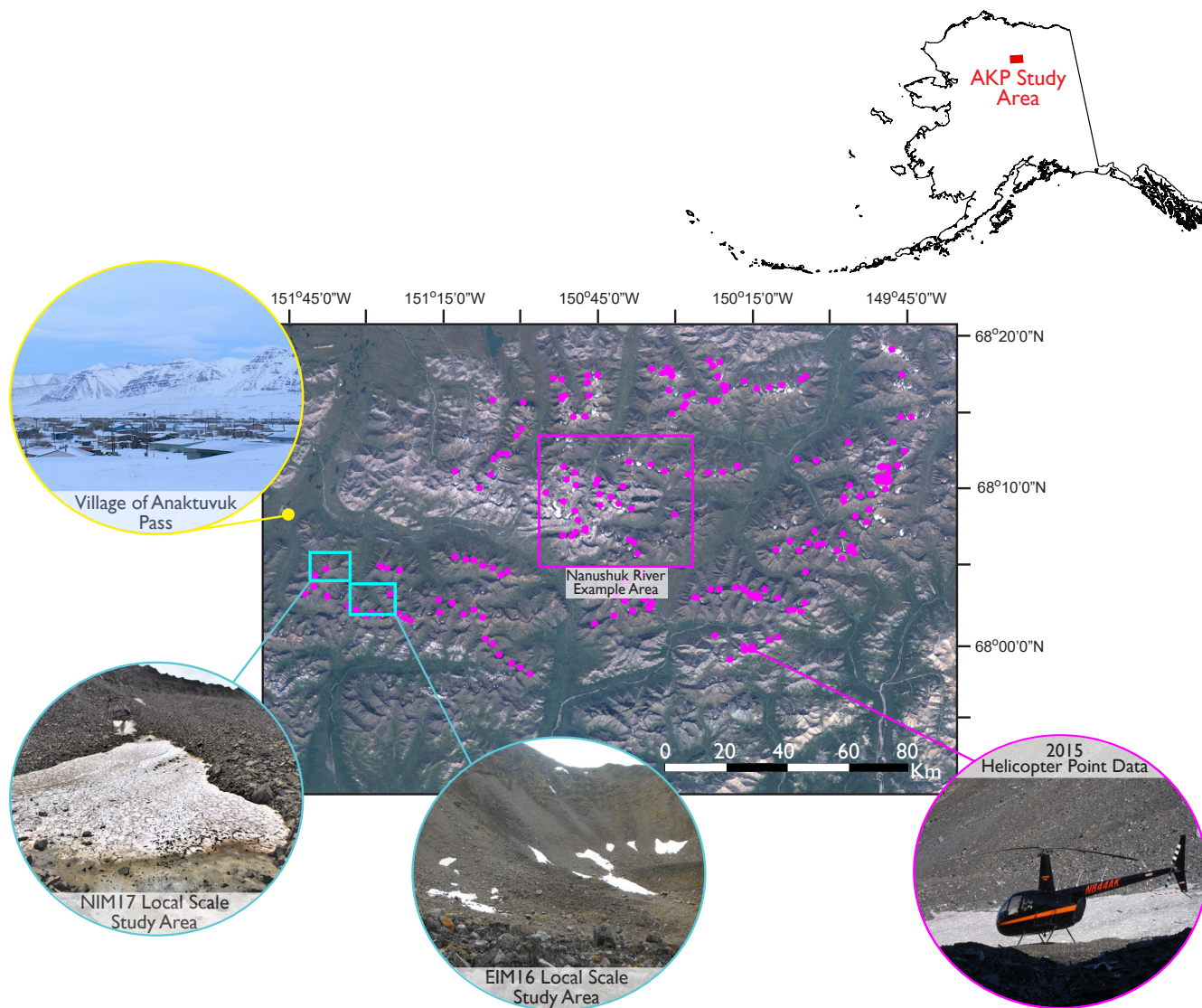


Figure 1. Study area map of the Anaktuvuk Pass (AKP) area in the Brooks Range, Alaska. Top left shows the location of AKP relative to the state of Alaska, USA. Bottom right shows a detailed AKP map derived from a Sentinel-2 cloud masked image generated in this study. Also seen are the locations of field collected data via helicopter fly-over points in 2015 and on-the-ground local scale field data collection sites. Local scale field sites include East Ingstad Mountain visited in 2016 (EIM16) and North Ingstad Mountain visited in 2017 (NIM17). The Nanushuk River Example Area is shown towards the middle of the AKP study area.



S1 C-band Level-1 Ground Range Detected (GRD) SAR backscatter in decibels (dB) is used to create the change detection algorithm, quantifying snowfield SCA for the same spatial extents and periods as S2 NDSI (2016-17 for mesoscale and local scale areas, 2016-19 across the Brooks Range). The S1 C-band SAR images are available in two single co-polarizations (HH: horizontal transmit / horizontal receive or VV: vertical transmit / vertical receive) and in two dual cross-polarizations (HH+HV: horizontal transmit / vertical receive or VV+VH: vertical transmit / horizontal receive). This study uses **VV** and VV+VH (herein referred to as **VH**); the bands typically used in SAR backscatter change detection for monitoring snow and ice (Nagler et al., 2016; Liang et al., 2021; Lievens et al., 2019 and 2021). The pixel (spatial) resolution for most bands in both S2 and S1 is 10m, except for S2 SWIR, which has a 20 m scale.

Also used in this study is a 10m resolution digital elevation model (DEM) for topographic corrections associated with mountain shadowing, SAR backscatter angles, as well as for a masking process eliminating unlikely elevations and slope angles from consideration for perennial snowfield coverage. This DEM, covering the Brooks Range study area, is taken from the 10m NASA Arctic Boreal Vulnerability Experiment (ABoVE) Composite DEM v2.1 (Burns et al., 2018). The NASA ABoVE Composite DEM is an aggregation of publicly available digital datasets into a single DEM that is free of voids.

The field collected data is used to ground truth remotely sensed locations and extents of some perennial snowfields. In summer 2015, Global Positioning System (GPS) data from a helicopter-supported survey were collected at almost 190 georeferenced points (*Figure 1*). Perennial snowfields were sighted at 160 fly-over points and at 27 touchdowns onto snowfields. Areas targeted during the helicopter campaign were based on minimum summer snow coverage identified using a Landsat-based snow persistence map for northwest Alaska (Macander et al., 2015). In summers 2016 and 2017, the field campaign was conducted on foot starting from the village of Anaktuvuk Pass. These datasets have a much smaller spatial extent than the helicopter survey, but a more robust spatial resolution. Detailed perimeters of a small number of perennial snowfields were obtained using a Real-Time Kinematic GPS (RTK-GPS) with sub-meter accuracy, in the local scale study areas EIM16 and NIM17 (*Figure 1*).

4 Methods

To evaluate the accuracy of the SAR-derived results, S1 SCA was compared to NDSI-derived SCA from S2 multi-spectral imagery. These remotely sensed products were also compared to field observed perennial snowfield locations and SCA. S1 and S2 imagery were accessed and analyzed using Google Earth Engine (GEE), a cloud-computing platform for planetary scale geospatial analysis (Gorelick et al., 2017). Each S1 scene was pre-processed in GEE for thermal noise removal and radiometric calibration (developers.google.com/earth-engine/guides/sentinel1). For S1 scenes in the Brooks Range study area, GEE applied a terrain correction using the NASA Advanced Spaceborne Thermal Emission and Reflection Radiometer (ASTER) DEM. In this study, additional corrections were also manually applied using the 10m NASA ABoVE Composite DEM v2.1 (Burns et al., 2018).

For both the S1 and S2 image analyses, two important steps were taken during pre-processing, and are similarly needed for SAR backscatter change detection (S1) and for NDSI (S2). The first of these is Simple Non-Iterative Clustering (SNIC), which



120 is an image partitioning algorithm used to grow super pixels. SNIC is applied to imagery before classifying to create results
with less of the “salt and pepper” effect of single outlier pixels due image complexity (Achanta and Susstrunk, 2017). The SNIC
technique is typically applied to multi-spectral images like S2, however, in this study, it was also applied to S1. The other pre-
processing step for S1 and S2 was a masking procedure that removed areas with no snow cover in summer, including surface
water (using NDWI), low elevations, and extreme slopes (using the DEM) (Tedesche et al., 2019). Also, larger glaciers located
125 in the Arctic National Wildlife Refuge (ANWR) in the Eastern Brooks Range that are not perennial snow, were identified
using the Global Land Ice Measurements from Space (GLIMS) (Cogley et al., 2015; GLIMS and NSIDC, 2018). For more
detailed descriptions of the pre-processing procedures and the approaches outlined in the following sections 4.1, 4.2, and 4.3,
see *Supplemental Material – S3.Extended Methods*.

4.1 Sentinel-2 NDSI Analysis

130 The first objective is to apply NDSI to the 10m resolution S2 TOA imagery to quantify perennial snowfield SCA in the AKP
mesoscale study area for the period of record from 2016 to 2019. To perform the terrain corrections and masking functions for
both S2 and S1, the 10m NASA ABoVE Composite DEM v2.1 (Burns et al., 2018) was utilized. Due to the limitations of multi-
spectral satellite imagery pertaining to distinguishing clouds from snow, an S2 modular cloud masking algorithm for the TOA
product was applied, using the 6-week summer season (1 July to 15 August) images to create a single cloud-free mosaicked
135 image for each year (2016 and 2017). The S2 TOA cloud masking process implemented *four modules*, based on GEE code
from Poortinga et al. (2019). These modules include: **(1)** mitigation of shadows (Housman et al., 2018); **(2)** mitigation of clouds
(Irish et al., 2006; Tedesche et al., 2019); **(3)** a bidirectional reflection distribution function (BRDF, Roy et al., 2017); and **(4)**
topographic illumination correction.

4.2 Sentinel-1 SAR Backscatter Change Detection Algorithm

140 The second objective is to derive an S1 SAR backscatter change detection algorithm to quantify perennial snowfield SCA
across the same spatial (AKP mesoscale area) and temporal (2016 to 2019) domains as in the first objective. Backscatter
values in each pixel of a single S1 scene manually selected from the summer study period of 1 July through 15 August were
differenced from those at the same location during the previous winter. Due to the location and orientation of the S1 swaths,
it was frequently necessary – choose two to four images and composite those to encompass the entire AKP study area, which
145 also served to lessen the effects of speckling, or granular interference inherent in SAR, which degrades image quality.

Winter reference images were created as a composite of ascending and descending orbit scenes from January of the same
year as the summer scene. An angular-based radiometric slope correction was also applied (Vollrath et al., 2020) to lessen
the effects of surface scattering on the backscatter signal, which is a significant issue in mountainous and complex terrain,
such as that of the Brooks Range (Small, 2011). The S1 SAR data are from the pre-processed Ground Range Detected (GRD)
150 collection in GEE, which does not include a radiometric slope correction. Therefore, this correction was applied using the
angular relationships between SAR images and terrain geometry derived from the ABoVE 10m DEM.



After pre-processing the S1 SAR data, the change detection between January composite reference images and summer images was implemented using an algorithm that considers the VV-polarized channel, the VH-polarized channel, and a combined VV- and VH-based channel using a weighting function that accounts for effects of the local incidence angle (Nagler et al., 2016). This algorithm exploits the backscatter attenuation occurring in wet snow, such as found in perennial snowfields during summer, compared to the lack of attenuation in the signal seen during the winter when snow is dry and the underlying ice is frozen. In each S1 pixel, the backscatter ratio between summer and winter images was calculated separately for VV and VH, as R_{VV} and R_{VH} , respectively (Nagler et al., 2016). Considering angular behavior, the following relation was applied for merging R_{VV} and R_{VH} ratios to create a combined single channel, R_C :

$$R_C = W * R_{VH} + 3 * (1 - W) * R_{VV} \quad \text{Eqn. (1)}$$

where the weight (W) varies depending on the local incidence angle (θ) of the terrain using the following rule:

If $\theta < 20^\circ$, then $W = 1.0$;

If $20^\circ \leq \theta \leq 45^\circ$, then $W = 0.5 * [1 + ((45^\circ - \theta) / 25)]$;

If $\theta > 45^\circ$, then $W = 0.5$;

This calculation, taken from Nagler et al. (2016), was modified slightly in this study. Employing a ratio technique with one polarization in the numerator and the other in the denominator (Nagler et al., 2016) did not yield good results in the S1 SAR data in the AKP study area. Artifacts from the mountainous terrain created strong noise signals that made it impossible to discern backscatter changes among the perennial snowfields when using the Nagler approach, even after the radiometric slope correction from Vollrath et al. (2020) was applied. Therefore, the polarization “ratio” calculated was the difference between subtracting the January composite VV_{ref} from the single image VV_{summer} and the VH_{ref} from the VH_{summer} , similar to the methodology outlined and implemented by Lievens et al. (2021). The VV backscatter ratio (difference) created a stronger contrast in the SAR images than that of the VH, so the VV portion of the change algorithm was given more weight and multiplied by a constant factor of 3. Resultant images were segmented using the SNIC process and a binary Otsu thresholding approach (Lv et al., 2020) was applied to find a dynamic threshold value unique to each image.

4.3 Field Evaluations

The third objective is an evaluation of results from the S1 change detection algorithm and S2 NDSI analysis by way of multi-resolution comparison with field collected data. A comparison was done between remotely sensed SCA (10m scale) and on-the-ground field collected SCA (sub-meter scale) in two small, local scale study areas in 2016 and 2017; East Ingstad Mountain (EIM16) and North Ingstad Mountain (NIM17), respectively (*Figure 1*). Areas of convergence were calculated, where perennial snowfields derived from S1 and S2 analyses, overlapped with snowfield areas measured in of the field. Also in 2016 and 2017, S1 and S2 results were compared to the field acquired helicopter point data from 2015 across the AKP study



area, by inspecting convergence between the remotely sensed snowfields with the field data. Two Cohen's Kappa coefficients (K) for 2016 and 2017, were calculated to find the relative agreement between the Sentinel and helicopter datasets (Vieira et al., 2010). Percent accuracies ($\% A$) were also calculated to find the relative agreement in co-location.

185 4.4 SAR vs. NDSI Comparison

The fourth objective is to compare results between the S1 SAR change detection and S2 NDSI analysis, for the full period of record (2016 to 2019). This was done within both the Nanushuk River example area and the AKP mesoscale study area. The Nanushuk River example area was used for visual representation of the results, since it is difficult to see the 10m resolution Sentinel results across the larger AKP study area. Calculations and comparisons of S1 SCA and S2 SCA for each summer
190 season from 2016 to 2019 were made, along with evaluations of areas of convergence between S1 and S2 results.

Results from the larger AKP study area for each year in each data set were then mapped. Because of the difficulty visualizing the 10m resolution Sentinel results, a grid with 250m x 250m cells was placed over the AKP area and percent coverage of perennial snowfield SCA was calculated within each grid cell. These representative percentages were used to map the S1 and S2 results for easier visualization. Some divergence between the total SCA calculations for S1 and S2 in the same study areas
195 and years was the result of the S2 cloud-masking process. Void spaces or areas of no data in the S2 mosaics were found and overlain onto the S1 data from the same year to see where snowfields may have been detected in the radar but not in the optical data due to consistent cloud cover. Where this was the case, the S2 data were combined with the portion of the S1 data of the same year that fell within the S2 void spaces. Another SCA metric was calculated by adding the S2 SCA with the S1 SCA in no-data areas of S2. Finally, areas of convergence between S1, and S2 plus S1, were calculated.

200 4.5 Four-Year Perennial Snowfields

The final objective is to map and quantify the four-year perennial snowfields persisting throughout the study period of 2016 to 2019. This was accomplished by combining the S2 NDSI and S1 SAR change detection results, for the AKP study area and across a domain that includes the entire Brooks Range. The NDSI multi-spectral technique for the S2 snowfield product and the S1 SAR change detection algorithm were extended beyond the AKP study area, and across the Brooks Range. Two (an S1
205 only and an S2 only), four-year perennial snowfield maps were created by finding snow-covered pixels that persisted across all four years of the study period in each product. Then, these eight images were stacked in GEE and each pixel was evaluated for snow persistence over the four years in parallel. The S2 product was given preference, as it had better agreement with the helicopter point data in the AKP area, but S1 areas of snow coverage were considered in places without S2 snow coverage as a possible location of cloud cover in S2.

210 A logical sequence was performed to determine if a pixel contained seasonal versus perennial snow. The sequence included the following evaluation to indicate perennial coverage: (1) if all four years of the S2 results contained snow, then the pixel was determined to be perennial; (2) if three years of S2 contained snow and one year did not, but had snow coverage in that same missing year in the S1 results, then that pixel was considered perennial; and (3) if two years of S2 contained snow and two years did not, but there was snow in those two same years of S1, then the pixel was considered perennial. All other combinations



215 of S2 and S1 were designated as non-perennial, indicating seasonal snow cover that may have persisted for only one or two
summers. As was the case with mapping snowfields in the AKP study area, the geographic extent of the Brooks Range is so
large that results from analysis of the 10m scale Sentinel data cannot be effectively visualized without a scaling factor. In this
case, a grid with 2km x 2km cells was placed over the Brooks Range and percent coverage of perennial snowfield SCA was
calculated within each grid cell for creating the maps.

220 5 Results

5.1 Sentinel-2 NDSI Analysis

NDSI was applied to the multi-spectral (optical) S2 TOA imagery to map and quantify perennial snowfield SCA in the AKP
mesoscale study area for the summer seasons of 2016 through 2019. Within the AKP study area, perennial snowfields derived
in the smaller Nanushuk River Example Area were mapped and quantified for better visualization purposes (*Figure 2*).

225 5.2 Sentinel-1 SAR Backscatter Change Detection Algorithm

Similar to the S2 NDSI approach, the S1 SAR backscatter change detection algorithm developed in this study was also im-
plemented to map and quantify snowfield SCA across the same spatial (AKP mesoscale area) and temporal (2016 to 2019)
domains. Results from the S1 analysis are included in the smaller Nanushuk River Example Area map (*Figure 2*), for a more
detailed visual representation compared to what can be seen in the larger AKP study area. Calculations of perennial snowfield
230 SCA derived from S1 and from S2 in the Nanushuk River area in 2016 were both equal to 28 km², while in 2017 they were 14
km² and 19 km², respectively (*Figure 2*). In 2018 and 2019, S1 and S2 SCA equaled 76 km² and 63 km², respectively (2018),
and 34 km² and 24 km², respectively (2019) (*Figure 2*).

5.3 Field Evaluations

To evaluate the accuracy of the S1 change detection algorithm, results of the S1 SAR-derived SCA were compared with field
235 collected data, as well as with NDSI-derived SCA from S2. In 2016 and 2017, S1 and S2 results were compared to 2015
field acquired helicopter point data across the AKP study area. This comparison was done on a per-pixel basis for every pixel
containing a helicopter point, by inspecting the convergence between remotely sensed snowfields derived from S1 and S2,
with the helicopter data (*Table 1*). Results of this comparison were used to calculate percent accuracies of the SCA detection
techniques and the Cohen's Kappa (*K*).

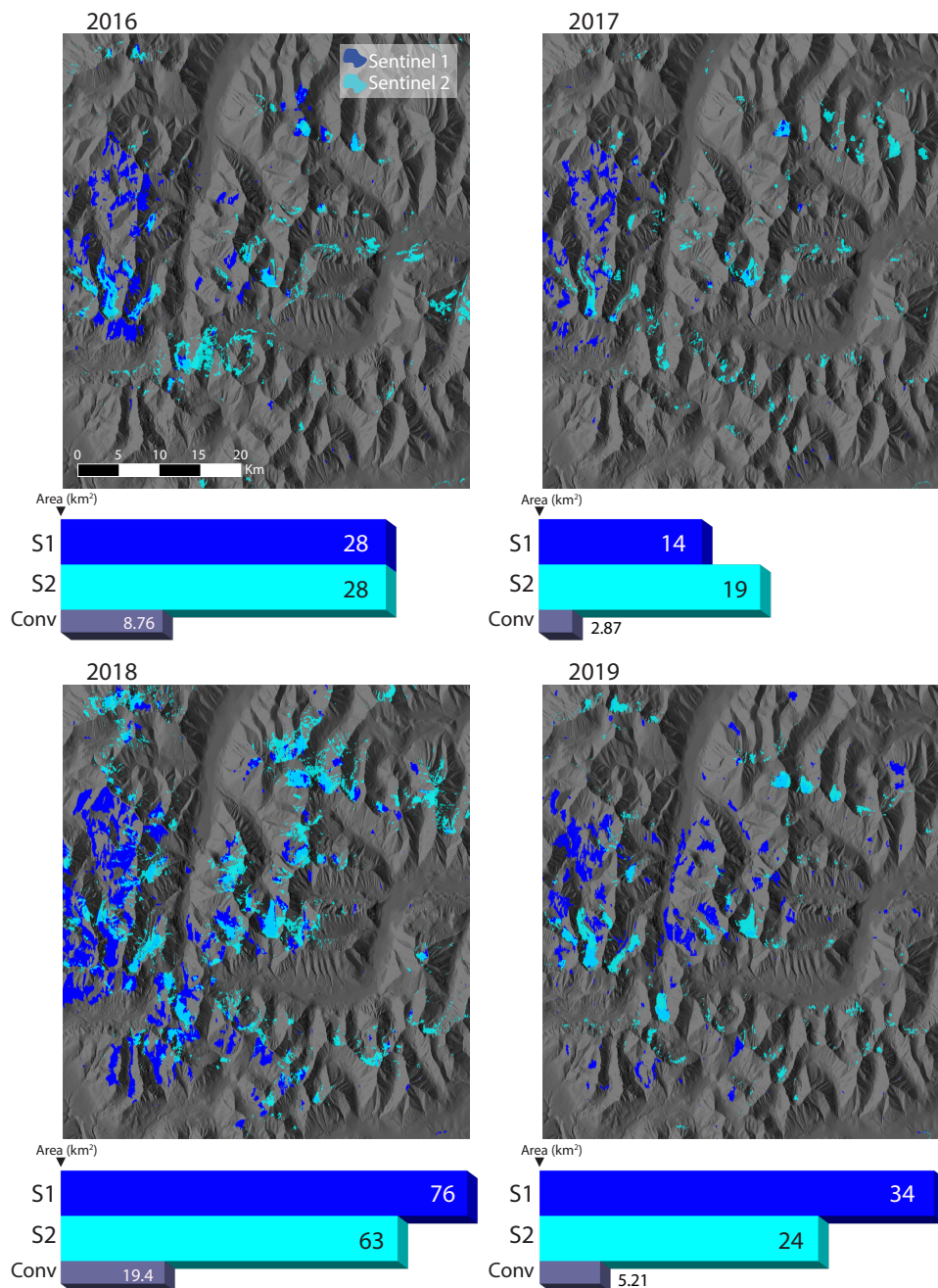


Figure 2. Nanushuk River Example Area perennial snowfields delineated and mapped from 2016 to 2019. The S1 SAR change detection algorithm results are in blue and the S2 NDSI-derived results are in cyan. Also shown are SCA totals for S2 and S1 in the Nanushuk River Example area, along with areas of convergence (overlap) between the datasets.



Table 1. Convergence of perennial snowfields found from 2015 field collected helicopter fly-over and touch down points with snowfields found from the S1 SAR change detection algorithm and from the S2 multi-spectral NDSI analysis in 2016 and 2017. Each dot indicates that there was convergence; meaning snow cover was present in the dataset in the same pixel as the helicopter point indicating snow cover.

2015		2016		2017		2015		2016		2017		2015		2016		2017			
Heli Pts	S1	S2	S1	S2	Heli Pts	S1	S2	S1	S2	Heli Pts	S1	S2	S1	S2	Heli Pts	S1	S2	S1	S2
1					49		●		●	97	●	●	●	●	145	●	●	●	●
2					50		●			98		●			146		●		●
3					51					99	●			●	147	●	●	●	●
4					52		●		●	100	●	●	●	●	148		●		●
5					53		●		●	101		●		●	149		●		●
6	●	●	●	●	54	●	●	●	●	102		●	●	●	150	●	●	●	●
7		●		●	55	●	●		●	103	●		●	●	151		●		●
8	●		●	●	56	●	●	●	●	104	●	●	●	●	152	●	●	●	●
9		●		●	57	●	●	●	●	105		●		●	153		●		●
10		●	●	●	58		●	●	●	106		●	●	●	154		●		●
11					59	●	●	●	●	107	●	●	●	●	155	●		●	●
12					60			●	●	108		●		●	156		●		●
13					61		●		●	109				●	157	●		●	●
14					62		●		●	110	●	●		●	158	●	●	●	●
15					63				●	111				●	159	●	●		●
16	●	●			64	●	●			112		●		●	160	●	●		●
17				●	65	●	●		●	113		●		●	161		●		●
18			●		66	●			●	114	●	●	●	●	162		●		●
19			●		67		●		●	115	●	●	●	●	163	●	●	●	●
20		●		●	68		●		●	116		●		●	164	●	●	●	●
21		●		●	69	●	●		●	117	●	●		●	165	●	●	●	●
22					70				●	118	●	●		●	166	●	●	●	●
23		●	●	●	71		●		●	119		●		●	167		●		●
24	●	●		●	72		●		●	120		●		●	168	●	●		●
25	●	●	●	●	73				●	121		●		●	169	●	●	●	●
26	●	●	●	●	74	●	●	●	●	122	●	●	●	●	170		●		●
27	●	●	●	●	75	●		●	●	123		●		●	171	●	●		●
28	●	●	●	●	76		●	●	●	124	●		●	●	172		●		●
29	●		●		77		●	●	●	125		●		●	173	●	●	●	●
30	●				78		●		●	126		●		●	174	●	●	●	●
31		●		●	79	●		●		127	●	●	●	●	175	●	●	●	●
32		●		●	80	●	●		●	128	●		●	●	176		●		●
33	●		●	●	81	●	●		●	129		●		●	177	●	●	●	●
34	●		●	●	82			●	●	130		●		●	178		●		●
35		●		●	83	●	●	●	●	131	●	●		●	179	●	●		●
36		●		●	84	●			●	132		●		●	180	●	●	●	●
37		●		●	85	●	●	●	●	133		●		●	181		●		●
38	●			●	86	●	●		●	134	●	●	●	●	182		●		●
39		●		●	87	●	●		●	135		●		●	183		●		●
40		●		●	88	●	●	●	●	136	●			●	184		●		●
41				●	89	●	●	●	●	137	●	●	●	●	185		●		●
42				●	90	●	●		●	138		●		●	186		●		●
43		●		●	91	●		●	●	139	●	●	●	●	187		●		●
44		●	●	●	92	●		●	●	140	●	●		●	188		●		●
45		●		●	93		●		●	141	●	●	●	●	189	●	●	●	●
46		●		●	94		●		●	142	●	●	●	●					
47		●	●	●	95	●	●	●	●	143	●	●	●	●					
48		●		●	96		●		●	144	●	●	●	●					



240 The results of the percent accuracy (% *A*) calculations for convergence of S1 and S2 SCA with helicopter fly-over and touch
down points (**Table 1**), include four values. For 2016 and 2017 in S1, percent accuracies are 44.4% and 36.0%, respectively,
and in S2, they are 78.8% and 82.5%, respectively. This indicates higher accuracy with the NDSI technique using optical
S2 imagery as compared to the SAR change detection technique using the S1 radar. Cohen's Kappa coefficient (**K**) analysis
of convergence between S1, S2, and the helicopter point data, resulted in values of 0.35 for 2016 and 0.69 for 2017. Cohen
245 suggested Kappa results be interpreted as: $K \leq 0$ means no agreement, $K = 0.01$ to 0.20 means slight agreement, 0.21 to 0.40
is fair, 0.41 to 0.60 is moderate, 0.61 to 0.80 is substantial, and 0.81 to 1.00 means perfect agreement (McHugh, 2012). The
Kappa coefficients in 2016 and 2017 indicate fair and substantial agreements, respectively.

Evaluation of results from the S1 change detection algorithm were also done using a multi-resolution comparison of snow-
field SCA in S1 and S2 (10m scale) with on-the-ground field collected SCA (sub-meter scale). This was done in the two focused
250 local scale study areas within the AKP area; EIM16 in 2016 and NIM17 in 2017 (**Figure 3**). The overall areas of manually-
collected perennial snowfield SCA in EIM16 and in NIM17 are 4,332 m² and 1,517 m², respectively (**Figure 3**). Calculations
of the areas of convergence between remotely sensed SCA and field collected SCA in EIM16 are 1,260 m² for S1 and 3,400
m² for S2. For NIM17, the areas of convergence are 960 m² for S1 and 900 m² for S2 (**Figure 3**). In 2016, the S1 radar and S2
optical datasets were able to detect about 30% and 80%, respectively, of the field-verified perennial snowfield SCA in the small
255 example area of EIM16. In 2017, S1 performed better than it did in 2016, while S2 performed worse, with detection rates of
about 63% and 60% of the field collected SCA, respectively, in NIM17.

5.4 SAR vs. NDSI Comparison

Comparisons were made between perennial snowfield SCAs calculated from the S1 SAR change detection and S2 NDSI
analysis for the period of record, within both the Nanushuk River Example area and the AKP mesoscale study area. In the
260 Nanushuk region, perennial snowfield areas of convergence (overlap) between the S1 and S2 results equaled 8.76 km² in 2016,
2.87 km² in 2017, 19.4 km² in 2018, and 5.21 km² in 2019 (**Figure 2**). This means that for the example area, the S1 SAR
change detection algorithm was able to pinpoint about 30% of the SCA identified using S2 NDSI thresholding in 2016. In
2017, 2018, and 2019, the S1 algorithm detected about 20%, 30%, and 22%, respectively, of the SCA found in the S2 results.

A third S2+S1 combination dataset for the larger AKP study area is compared to the S1 only and S2 only results in **Figure**
265 **4**. While in **Figures 2** and **3**, the perennial snowfields seen directly represent SCA, in **Figure 4**, they are represented as a
percentage of snow cover per 250m x 250m grid cell. This was done for better visualization of the perennial snowfields across
the large AKP area. Calculations of SCA and convergences in the AKP area were still performed using the simple raw area, as
was done in the local scale and Nanushuk River areas (**Figure 5**). Total SCA calculations in AKP for S1, S2, S2+1, and their
convergences, are also seen in **Table 2**.

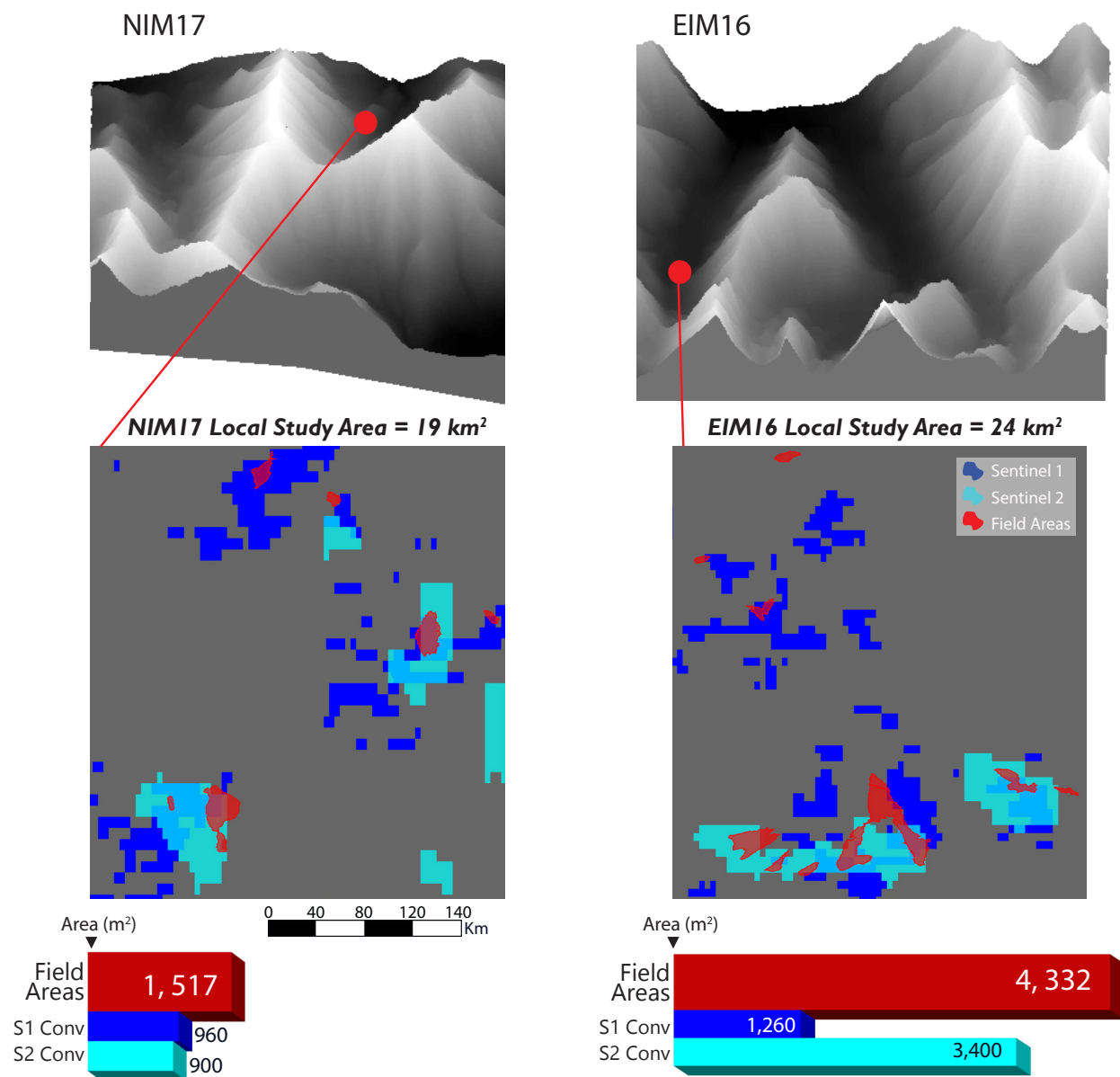


Figure 3. Results of the multi-resolution comparison of SCA from S1 and S2 with field collected SCA in two focused study areas. North Ingstad Mountain (NIM17, *left*) and East Ingstad Mountain (EIM16, *right*) local scale areas. Topography for each area is shown on top. Focused sample areas show sub-meter resolution, on-the-ground field collected perennial snowfield SCA mapped in red, with 10 m x 10 m S1 (blue) and S2 (cyan) SCA. Below the maps, total SCA calculations for the field data are shown with convergence areas for S1 and S2.

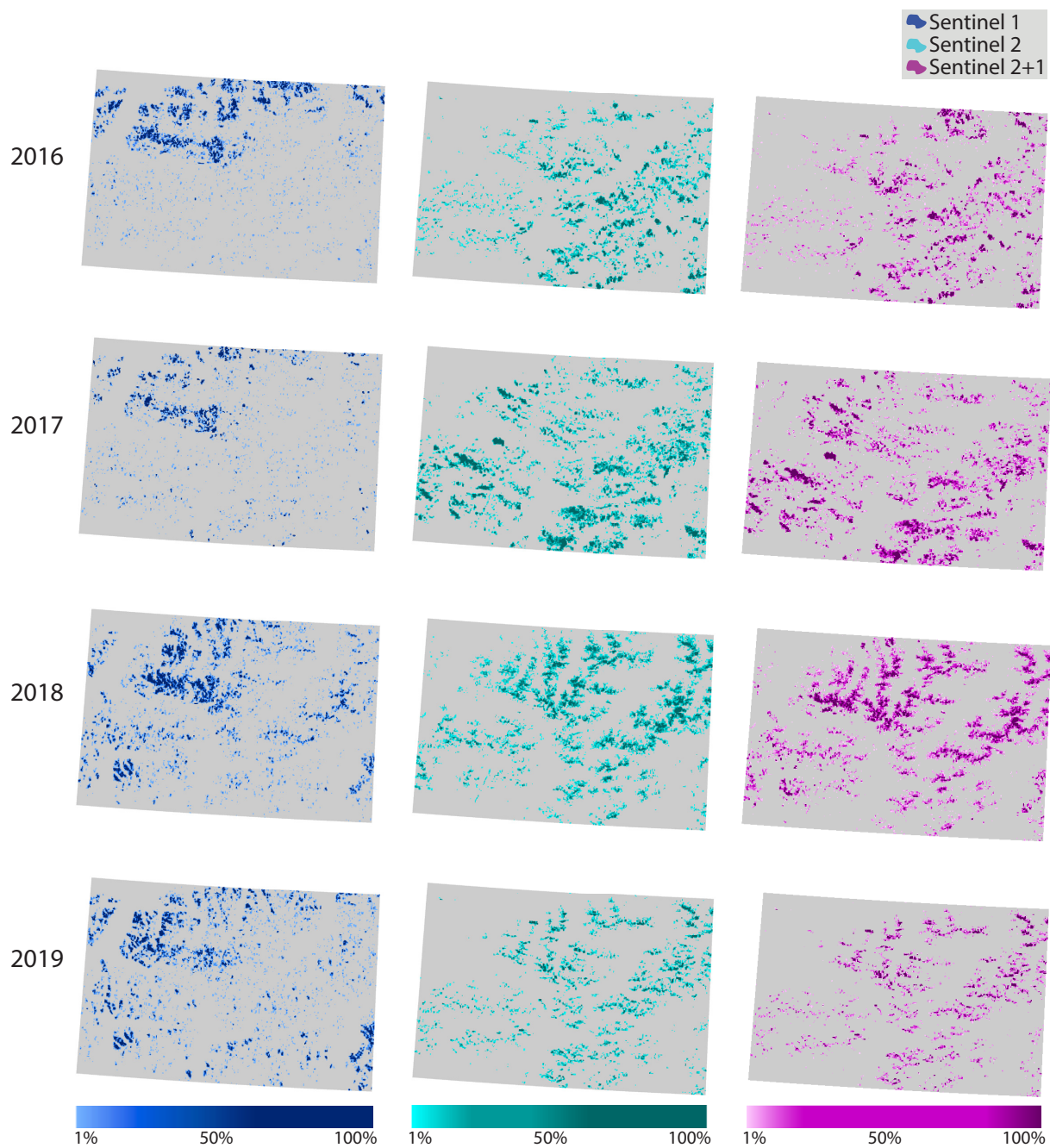


Figure 4. Perennial snowfield SCA results from the S1 change detection (*first column*) and the S2 NDSI analysis (*second column*) are shown for the full period of record from 2016-2019 in the AKP study area as percent coverages per 250 m x 250 m grid cell. In the *third column*, S2 results are combined with the portion of S1 results of the same year that fell within cloud masked void spaces in the S2 results.

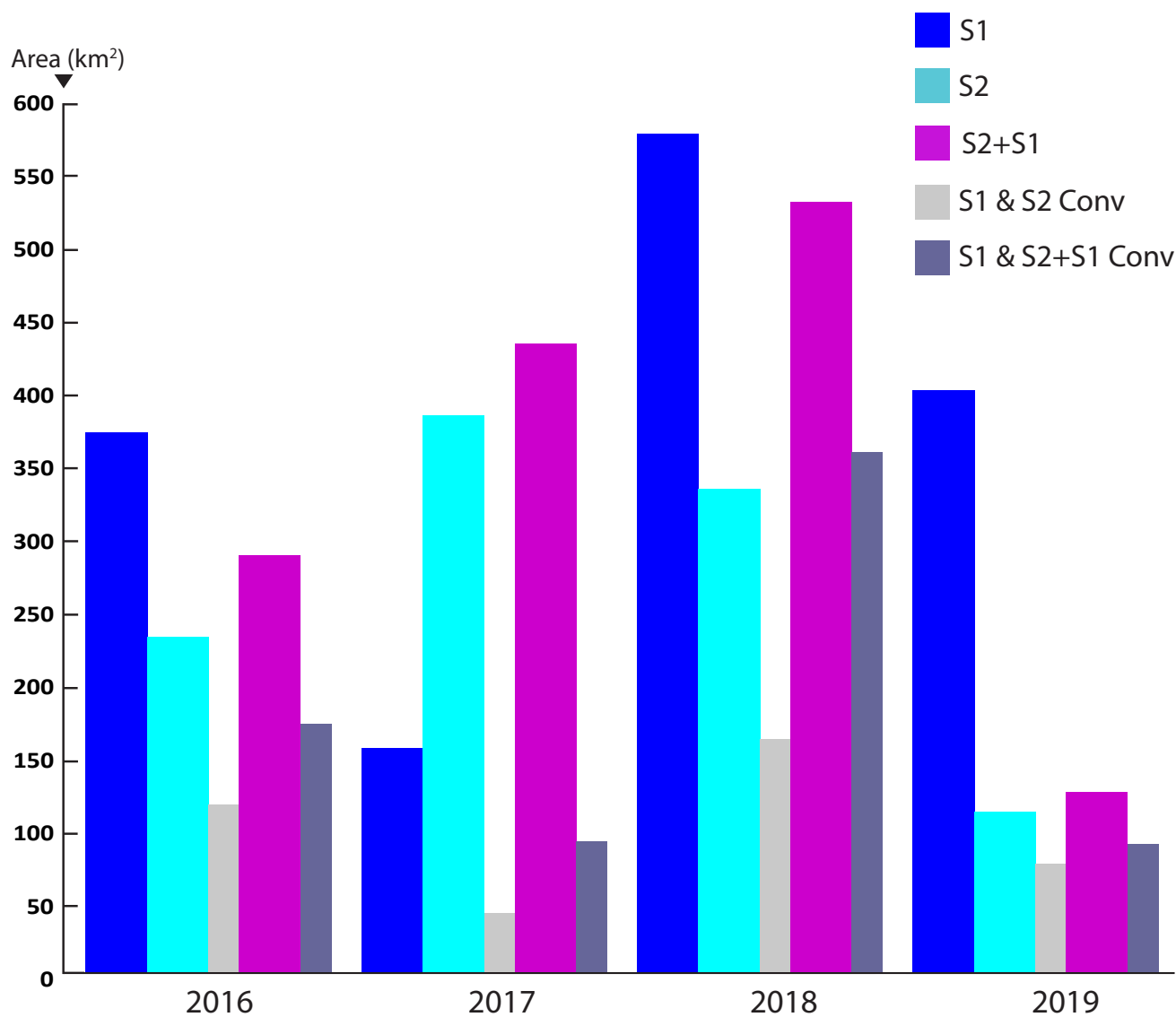


Figure 5. Total SCA calculated from the S1 SAR change detection algorithm (S1), the S2 NDSI analysis (S2), and from S2 results combined with S1 results of the same year that fell within cloud masked voids in S2 (S2+S1). SCA totals were calculated within the AKP study area for each summer season during the study period of record (2016-2019). Also shown are areas of convergence (overlap) between S1 and S2, and between S1 and S2+S1.



Table 2. SCA results in km² in the AKP study area from the S1 SAR algorithm (*S1*), the S2 NDSI analysis (*S2*), S2 with S1 filling in the cloud voids (*S2+S1*), and convergences between the data sets.

Summer Season	S1 (km ²)	S2 (km ²)	S2+S1 (km ²)	S1 and S2 Convergence (km ²)	S1 and S2+S1 Convergence (km ²)
2016	394	253	309	137	193
2017	176	406	455	63	112
2018	600	355	553	182	380
2019	423	132	146	96	110

270 The convergent areas in AKP indicate that the S1 SAR change detection algorithm was able to find 54% of the SCA identified in the S2 NDSI results in 2016 and 62% of the SCA in the S2+S1 combination dataset, also in 2016 (*Figure 5, Table 2*). In 2017, 2018, and 2019, the S1 algorithm detected 16%, 50%, and 73%, respectively, of the SCA found in S2 of the corresponding year, as well as 25%, 70%, and 75%, respectively, of S2+S1 SCA of the same year (*Figure 5, Table 2*).

5.5 Four-Year Perennial Snowfields

275 The last step of this study involved generating maps of perennial snowfields that persisted in all four years of the study period and quantifying their SCAs, within the AKP study area and across a large domain, which includes the entire Brooks Range. Three maps were created for the Brooks Range, with the AKP area highlighted, including an S1 SAR only map of four-year perennial areas, an S2 only map, and a map which combines S2 and S1, with S2 as the basis supplemented by S1 (*Figure 6*). As with *Figure 4*, perennial snowfields in *Figure 6* are represented as a percentage of snow cover per grid cell (2km x 2km).
 280 Calculations of SCA and convergences were performed using the simple raw area (*Figure 6, Table 3*).

For the four-year perennial snowfields, the convergent areas in AKP indicate that using the S1 SAR change detection algorithm alone to find longer term persistent snowfields captured 28% of those found using S2 NDSI alone and about 20% of the S2+S1 combination approach (*Figure 6, Table 3*). The convergent areas across the full extent of the Brooks Range show that using the S1 SAR results alone captured about 23% of the longer term persistent SCA found using S2 only and 28% of S2+S1
 285 (*Figure 6, Table 3*). On the basis that the S2+S1 approach is most accurate, we estimate that the overall area of perennial snowfields during the 2016 to 2019 time period was 18.4 km² in the AKP study area and 385 km² across the full extent of the Brooks Range.

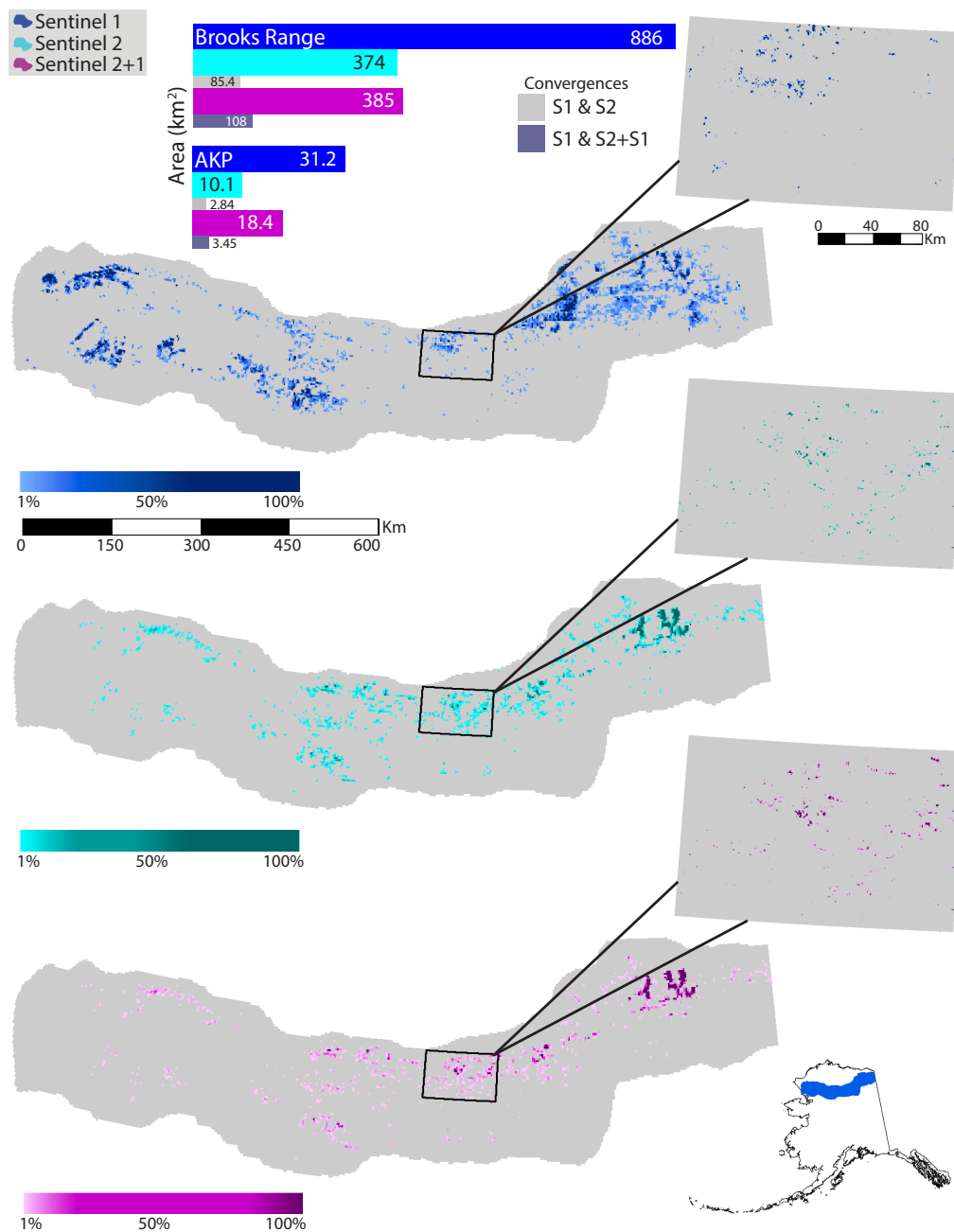


Figure 6. Four-year perennial snowfields persistent for 2016-19 period in AKP and Brooks Range areas, as percent coverages per 250 m x 250 m and 2 km x 2 km grid cell, respectively. S1 (*top*) and S2 (*middle*) snowfields were found from snow-covered pixels persistent in all years. S2+S1 (*bottom*) snowfields are a combination of S2 and S1, including: (1) persistence in all years of S2, (2) persistence in three years of S2 and in S1 of missing S2 year, and (3) persistence in two years of S2 and in S1 of both missing S2 years.



Table 3. Four-year perennial snowfield SCA persistent for the 2016-19 period in km² across the entire Brooks Range and within the AKP study area; results from S1 SAR algorithm only (*S1*), S2 NDSI analysis only (*S2*), S2 with S1 to fill in missing years (*S2+S1*), and convergences between the data sets.

Spatial Extent	S1	S2	S2+S1	S1 and S2 Convergence	S1 and S2+S1 Convergence
	(km ²)	(km ²)	(km ²)	(km ²)	(km ²)
AKP	31.2	10.1	18.4	2.84	3.45
Brooks Range	886	374	385	85.4	108

6 Discussion

6.1 Sentinel-2 NDSI Analysis

290 When NDSI was applied to S2 TOA imagery to quantify perennial snowfield SCA in the AKP area, the cloud masking procedures, which involved topographic corrections and the mitigation of clouds and shadows, minimized pixels with no data for the summer seasons from 2016 through 2019, but did not completely eliminate them. Therefore, a third remotely sensed data set, in addition to S2 NDSI and S1 SAR change detection, was generated by finding the no-data areas (void spaces) in S2 that were artifacts of the cloud-masking optical mosaicking process (*Figure 4*). These void spaces were filled with S1 data of the same
 295 year and matching pixel, where S1 indicated that there was a snowfield present. The S2 results were chosen as the primary dataset for this combination, with S1 results as a supplement in the no-data areas, because the S2 results yielded higher percent accuracies during the evaluation with the field-acquired helicopter point data. S2 also performed slightly better at the local scale evaluation, where areas of convergence with manually collected SCA were nearly equal between S1 and S2 in 2017, but higher in S2 than S1 in 2016, indicating more agreement between S2 and the field data (*Figure 4*).

300 Paul et al. (2016) found snow cover extents derived from Landsat 30m bands to be 4%–5% larger than S2, indicating a more generous interpretation of mixed pixels. They found that mapping of snow cover with S2 provided accurate results but believe that the required topographic correction would benefit from a better orthorectification with a more precise DEM. Paul et al. (2016) used the 30m ASTER GDEM Version 2. In our study, it was also found that some individual snowfields detected in S2 were larger than those from the same year in S1; however, overall S1 appears to overestimate SCA in comparison to S2. The
 305 DEM used in our study, the 10m ABoVE DEM, has a finer spatial scale than ASTER V2 and may be more accurate than that used by Paul et al. (2016). This may yield more accurate results during implementation of both S2 topographic corrections and S1 angular-based radiometric slope correction (Vollrath et al., 2020).



6.2 Sentinel-1 SAR Backscatter Change Detection Algorithm

The need for a cloud-cover independent approach to detecting and quantifying perennial snowfields with remotely sensed im-
310 agery is especially salient in the Brooks Range, as this area of the Alaskan Arctic is frequently covered with dense clouds. These
clouds form at the interface between the Arctic Ocean and North Slope of Alaska (Zhang et al., 1996) and move unencumbered
across the open flat tundra until they are stopped by the orographic barrier created by the Brooks Range (Mülmenstädt et al.,
2012). This study was conducted to develop a remote sensing technique to overcome some of these limits presented by cloud
cover. By adapting SAR backscatter change detection methods employed in previous studies for delineating melt areas within
315 seasonal snow and on perennial ice, a SAR algorithm was created specifically for finding perennial snowfields in our study
area (Strozzi et al., 1997; Bernier et al., 1999; Nagler et al., 2016; Lievens et al., 2019; Liang et al., 2021).

The ability of the S1 SAR algorithm to detect perennial snowfields varied, although results tended to improve in later years.
Detection rates by S1 as a percentage of field collected SCA in the two local scale study areas improved between 2016 and
2017, going from 30% to 63% of the field verified SCA (**Figure 3**); however, S1 SCA detection rates as a percentage of the S2
320 NDSI analysis results in the Nanushuk River example area stayed relatively constant across the four-year study period of 2016
to 2019, ranging from 20% to 30% (**Figure 2**). S1 detection rates as a percentage of S2 and of S2+S1 in the larger AKP study
area also generally improved over the progression of the study period. S1 detection rates in AKP for S2 and S2+S1 in 2016
ranged from about 50% to 60%, while 2017 through 2019, the rates ranged from about 20% to 75%, with an improvement in
each subsequent year (**Figures 4 and 5, Table 2**). This may be related to the increase in availability of SAR images over the
325 Brooks Range in each subsequent year of the study period. In 2015 and 2016, S1 coverage over Alaska was temporally limited
(Potin et al., 2016), as compared to 2018 and 2019, with the launch of the second Sentinel-1 satellite. Sentinel 1B alternates
return times with the original Sentinel-1A, generating more SAR images over the same period (Schwerdt et al., 2017).

In the S1 change detection procedure, resultant images of combined VV and VH bands were thresholded with the Otsu
technique to find values unique to each S1 image. Previous SAR change detection algorithm studies, including Nagler et
330 al. (2016) and others, simply and effectively used a -2 dB threshold standard for finding wet snow in the backscatter ratio
images. This approach did not work well in our study, potentially because VV_{ref} and VH_{ref} were subtracted from VV_{summer}
and VH_{summer} , respectively, rather than used in a ratio, as was done by Nagler et al. (2016). In this study, the two backscatter
values were subtracted, as was done by Lievens et al. (2021). This resulted in backscatter values that were easier to interpret
and threshold.

335 Methods explored in this study, but ultimately not implemented, included the removal of early morning S1 images before
deriving changes in the backscatter values between the winter reference image and the summer images. This approach did
not seem to add accuracy to the S1 snowfield SCA estimates. Times of day when perennial snowfields might be colder, and
possibly frozen, during summer seasons would be close to the middle of the night or in the early morning. The angle of diurnal
solar radiation in the study area does not change substantially during the summer, as the Brooks Range is located above the
340 Arctic Circle; however, there are slight changes to the angle of the sun in early and late summer, and when combined with steep
mountainous terrain, some shadowing does still occur. This shadowing may allow for some freeze-melt cycling of snowfield



outer layers, and ice does not attenuate SAR backscatter in the same way as wet firn on snowfields (Rott and Mätzler, 1987; Floricioiu and Rott, 2001). In the AKP study area, all S1 images are taken from 6am to 7am AKST (15:00 to 16:00 UTC) or 5pm to 6pm AKST the day before (02:00 to 03:00 UTC). Ultimately, removing the 16:00 UTC images on the assumption that snowfields could be frozen at 7am did not produce a detectable improvement in the results.

6.3 Field Evaluations

There are three levels of accuracy from which to evaluate the results of the S1 change detection algorithm analysis. These levels include ground-based surveying at sub-meter accuracy (*Figure 3*), S2 NDSI derived SCA data at a 10m resolution, and field collected helicopter point data (*Figure 1*), which are very accurate, but have a coarse scale. Although on-the-ground field data sets have limited spatial coverage, they contain a robust level of detail in a fine spatial scale. At this level of accuracy, the S1 and S2 datasets have good agreement (convergence) with field data in NIM17; however, in EIM16, only S2 has fairly good agreement with the field data (*Figure 3*). The areas of convergence between both Sentinel data sets generally show that either S2 underestimates SCA, or S1 overestimates. In both 2016 and 2017, the S2 NDSI results converge more frequently with the 2015 helicopter point data than results from the S1 change detection algorithm, although both S1 and S2 have fairly good overlap with the point data (*Table 1*).

Field collected SCA in the local scale study areas (*Figure 3*), is a small sample of perennial snowfields in the AKP area overall, as field work in remote locations of the Brooks Range is logistically challenging. Therefore, there may have been a number of other locations where the manually collected and remotely sensed SCA would have aligned either worse or better. This sample indicates that remotely sensed SCA in both S1 and S2 are at least in the vicinity and/or adjacent to, SCA found in the field (*Figure 3*). Some misalignments between the remote sensing results and the field collected data could be from thresholding errors in SAR backscatter change and in NDSI. These approaches may need further experimentation with additional years of Sentinel imagery. Also, some disagreements between S1, S2, and the manually collected SCA may be related to inherent differences in snow measurement scaling, which previous studies have shown are not easily resolved (Fassnacht and Deems, 2005; Fassnacht et al., 2016; Tedesche et al., 2017).

6.4 SAR vs. NDSI Comparison

One consistent observation is that the S1 results indicate that more snowfields are present than the S2 results. Only in 2017 did S2 estimate more SCA than S1 (*Figures 2 and 4*). One explanation is that S2 is underestimating SCA because of missing data or voids as a result of the cloud masking process, which cannot find a value for individual pixels if every image during the summer season has a cloud present (Poortinga et al., 2019; Stillinger et al., 2019). This is only a partial explanation for the divergence, however. The S2+S1 combined datasets for each year typically increased S2 SCA totals and brought them closer to S1 SCA totals (*Figure 5, Table 2*), but S1 still indicates more SCA than S2+S1. In 2016 and 2018, S2+S1 SCAs were notably larger than S2 alone and closely aligned with SCA calculations in S1, with additional SCA values in the S2 voids equaling 56 km² and 198 km², respectively (*Figure 5, Table 2*). In 2017, S2 was larger than S1 and in 2019, there were almost no S2 voids. Therefore, S2 and S2+S1 were nearly the same in 2019, with only a 14 km² increase from S2 to S2+S1 (*Figure 5, Table 2*).



375 After close inspection of the raw radar backscatter change results, it was also observed in S1 that results of the SAR algorithm
sometimes detects only a portion of a perennial snowfield. This portion is typically the outer perimeter. This is possibly because
the outer edges of perennial snow and ice might be the warmest and wettest parts during the summer. It was expected that the S1
radar signal would be attenuated across the entire surface of each snowfield in the summer, as the surface would be isothermal,
while the inside may still be fully frozen. The dielectric properties of liquid water change the strength and angle of radar
backscatter signals (Barker and Watts, 1973), and therefore, reduces the backscatter coefficient (σ^0) of wet snow (Evans, 1965;
380 Tiuri et al., 1984). In other words, the σ^0 coefficient of snow decreases with increasing liquid water content (Shi and Dozier,
1995; Ulaby and Long, 2014); however, it appears that sometimes the attenuation is so small that the change in radar backscatter
values is outside of the threshold and therefore not detected as snow. These areas of the snowfields might be more frozen than
expected in mid-summer, containing only a small amount of liquid water.

385 Notably, it was observed in some areas that the magnitude of difference in backscatter, measured in dB, between the summer
images and the winter reference image, were greatest around the edges or perimeter of certain perennial snowfields and then
the magnitude of backscatter differences gradually decreased towards the center of the snowfield. Detailed manual inspection
reveals instances where S1 and S2 are each detecting the same perennial snowfield, but for different areas (**Figures 2 and 5,**
Table 2). This may be because S1 SAR change detection is sensitive to liquid content of the snowfields (Tiuri et al., 1984),
390 while S2 NDSI is sensitive to the optical properties of the snowfields, such as reflectance or albedo (Naegeli et al., 2017).
Therefore, it may be a more effective approach to not only count areas of convergence where S1 and S2 snow covered pixels
directly overlap, but also within a defined spatial proximity of each other via a statistical filter or spatially weighted boundary
area as was done in Li et al. (2013).

Another explanation for the divergence in spatial coverage of perennial snowfields indicated by the S1 SAR change detection
395 algorithm versus the S2 NDSI multi-spectral method, may be related to the thresholding technique employed in the SAR
algorithm. This technique involves a binary Otsu thresholding approach (Lv et al., 2020), which is dynamic and dependent on
the size of the area being considered. Also, both S1 and S2 imagery were processed using a scale dependent SNIC segmentation
process (Hirayama et al., 2019). In this study, SNIC noticeably improved the results in both S2 and S1 by eliminating outlier
pixels; however, SNIC combined with a dynamic thresholding technique such as Otsu, may have caused some errors in the
400 thresholding of the SAR backscatter change values. Many experimental runs of both the S1 SAR algorithm and S2 NDSI
technique were performed with various values for the SNIC input parameters, such as compactness, and the final input values
were chosen based on manual inspection. Overall, S1 still identifies major clusters of snowfields in the same locations as S2,
but individual SCA values differ when comparing S1 to S2.

Divergences between S1 and S2 could also be an artifact of the angular-based radiometric slope correction applied to the
405 S1 imagery (Vollrath et al., 2020). This terrain correction algorithm greatly improved the results of the S1 backscatter change
detection across the mountainous terrain of the Brooks Range. Dramatic changes in slope angle have a significant impact on
the return angle or local incidence angle of the radar backscatter (Floricioiu and Rott, 2001). This slope correction, while
accounting for the majority of terrain effects, may still not be enough of a correction to eliminate all effects of very steep
mountains completely (Small, 2011).



410 The SCA in the AKP study area detected by the S1 SAR change detection algorithm decreased from 2016 to 2017 (**Figures**
2, 4, 5), a finding which agrees with previous studies that show an overall decreasing trend in perennial snowfield coverage
in the Brooks Range over the last several decades (Tedesche et al., 2019). However, the S1 decrease from 2016 to 2017 was
by more than 50%, which is substantial and indicates that some of the snow classified in 2016 as perennial may have been
persistent seasonal snow cover left after a high snowfall winter (Gardelle et al., 2013; Brun et al., 2017). A one or two year
415 increase in the size of perennial snowfields from persistent snow cover will add to the firn and superimposed ice mass over the
short-term, however, Tedesche et al., 2019 uses a working definition of perennial as a minimum of four years of persistence.
In contrast to the S1 reduction in SCA from 2016 to 2017, SCA found by the S2 NDSI results increased from 2016 to 2017.
This discrepancy could be due, as discussed above, to several factors, including data voids in S2 resultant of cloud masking
algorithms that are necessary to evaluate snowfield coverage in optical imagery. During the creation of the S2+S1 datasets
420 (**Figures 4 and 5**), areas of cloud voids in the S2 mosaics were quantified. In 2016 and 2017, these voids were 2,470 km² and
1,582 km², respectively, in the AKP area. This likely explains why S2 SCA was lower in 2016 than in 2017 in the AKP area,
while it was the opposite for S1.

6.5 Four-Year Perennial Snowfields

The S1 derived four-year perennial snowfields might be an overestimate of overall SCA across the Brooks Range, as S1 only
425 four-year snowfields in AKP align more closely with S2 only and S2+S1 combined in the AKP area (**Figure 6**). The S2 only
and S2+S1 combined four-year perennial snowfield maps are quite similar in both the Brooks Range and AKP study areas,
although there is noticeably more SCA in AKP for S2+S1 than for S2 alone in AKP (**Figure 6, Table 3**). All three maps of the
Brooks Range, including the more divergent S1 only map, detect the highest concentrations or clusters of perennial snowfields
in the same general regions across this mountain range, although percent coverage values within those regions vary.

430 While perennial snowfields persist over multiple years and remain stable over the summer seasons, inter-annual variability
in minimum snow cover extents can complicate mapping and quantifying snowfield extents. Much inter-annual and seasonal
snow cover variability is seen in the AKP study area during the period of record (2016-2019), even during the summer when
seasonal snow has less influence. Perennial snowfields are sensitive to temperature and precipitation, and will expand or con-
tract according to climatic conditions, representing change in climate over time. In exceptionally warm years, it is conceivable
435 to expect large changes in the margins. Inter-annual variability has also been noted in other studies of perennial snow and ice;
in reconstructions and time series of mass balance calculations of glaciers (Gardelle et al., 2013; Brun et al., 2017). Also, there
are inherent, or at least potential, divergences in SCA represented by the remotely sensed versus field collected data, due to
differences in spatial scaling (Grünwald et al., 2010; Fassnacht et al., 2020).

7 Conclusion

440 The Sentinel-1 (S1) SAR backscatter change detection algorithm and Sentinel-2 (S2) optical imagery, analyzed using the multi-
spectral NDSI approach, both effectively detect perennial snowfield locations in the Brooks Range of Alaska. However, both



also capture inter-annual variability in seasonal snow cover persisting over a single summer season. When multiple years of S1 and S2 results are combined and only pixels with snow cover persisting across all years are mapped, much of the seasonal variability is eliminated. Consistently, S1 estimates more SCA than S2 in a given year, which may be due to areas of missing
445 data (voids) in S2 from the cloud masking process required to implement NDSI. When voids in the S2 results were identified and filled with spatially and temporally matched S1 SAR results, SCA calculations of S2+S1 more closely aligned with S1.

S1 and S2 may be detecting different portions of the same perennial snowfields in some instances. Magnitudes of differences in SAR backscatter values sometimes varied over the surface of the same snowfield in the S1 data, possibly due to variations in liquid water content. Radiometric terrain correction was critical in this mountainous study area, however, there may still be
450 some errors in the SAR results due to steep terrain. Overall, both S1 and S2 identified the same clusters of snowfields, but SCA estimates within the clusters were typically larger in S1. The motivation for this work is to inform subsistence hunters in the Brooks Range of Alaska and other stakeholders in the Arctic, interested in how the ecosystems that they work and live in are affected by changes in perennial snowfields.

Code Availability

455 Code for deriving perennial snowfield extents in the Brooks Range using the S1 SAR backscatter change detection algorithm:
<https://code.earthengine.google.com/3d0eb217a3e6b2655c471d2778f26833>

Code for thresholding S1 SAR backscatter change detection results:

<https://code.earthengine.google.com/e5163f9ceafedcba99a642c53c5550e1>

Code for deriving perennial snowfield extents in the Brooks Range using NDSI and S2 multi-spectral imagery:

460 <https://code.earthengine.google.com/88ca5581068fecc38f0244f65a4459bc>

Code for angular-based radiometric slope correction of S1 (Vollrath et al.,2020):

<https://github.com/ESA-PhiLab/radiometric-slope-correction>

Code modules for cloud masking of S2 (Poortinga et al.2019):

<https://mygeoblog.com/2018/10/24/modular-landcover-system-for-sentinel-2/>

465 Data Availability

Sentinel-1 (S1) and Sentinel-2 (S2) image collections are available via Google Earth Engine:

<https://developers.google.com/earth-engine/datasets/catalog>



Author Contribution

All authors contributed to the conceptual design and technical structure of the research. Analysis, coding, literature review, field data collection, and figure development was performed by MT. All authors contributed to the interpretation of the results. MT wrote the paper with regular guidance and editing provided by ET, SF, and GW.

Competing Interests

The authors declare that they have no conflict of interest.

Acknowledgements

This research was funded by a NASA Earth and Space Science Graduate Fellowship (NESSF), a Pathfinder Fellowship from the Consortium of Universities for the Advancement of Hydrologic Science, Inc.(CUAHSI), an Explorer’s Club Grant, an NSF Experimental Program to Stimulate Competitive Research (EPSCoR) Grant, a NASA Alaska Space Grant Program Fellowship (ASGP), financial contributions from the Alaska Center for Climate Assessment and Policy (ACCAP), and an American Water Resources Association Fellowship (AWRA).

We are grateful for the support from these grantors, for the support of Gates of the Arctic National Park and Preserve, and for our volunteer field assistants. We also acknowledge that this work was on the ancestral hunting grounds of the Nunamiut and Iñupiaq peoples and are grateful for their centuries of stewardship of these lands.



References

- Achanta, R. and Susstrunk, S.: Superpixels and Polygons Using Simple Non-iterative Clustering, in: 2017 IEEE Conference on Computer Vision and Pattern Recognition (CVPR), 2017 IEEE Conference on Computer Vision and Pattern Recognition (CVPR), Honolulu, HI, 485 4895–4904, <https://doi.org/10.1109/CVPR.2017.520>, 2017.
- Anderson, J. R. and Nilssen, A. C.: Do reindeer aggregate on snow patches to reduce harassment by parasitic flies or to thermoregulate?, *Rangifer*, 18, 3–17, <https://doi.org/10.7557/2.18.1.1369>, 1998.
- Barker, J. A. and Watts, R. O.: Monte Carlo studies of the dielectric properties of water-like models, *Molecular Physics*, 26, 789–792, 1973.
- 490 Bernier, M., Fortin, J.-P., Gauthier, Y., Gauthier, R., Roy, R., and Vincent, P.: Determination of snow water equivalent using RADARSAT SAR data in eastern Canada, *Hydrol. Process.*, 13, 3041–3051, [https://doi.org/10.1002/\(SICI\)1099-1085\(19991230\)13:18<3041::AID-HYP14>3.0.CO;2-E](https://doi.org/10.1002/(SICI)1099-1085(19991230)13:18<3041::AID-HYP14>3.0.CO;2-E), 1999.
- Berrisford, M. S.: Evidence for enhanced mechanical weathering associated with seasonally late-lying and perennial snow patches, Jotunheimen, Norway, *Permafrost and Periglacial Processes*, 2, 331–340, <https://doi.org/10.1002/ppp.3430020408>, 1991.
- 495 Brighenti, S., Hotaling, S., Finn, D. S., Fountain, A. G., Hayashi, M., Herbst, D., Saros, J. E., Tronstad, L. M., and Millar, C. I.: Rock glaciers and related cold rocky landforms: Overlooked climate refugia for mountain biodiversity, *Global Change Biology*, 27, 1504–1517, 2021.
- Brun, F., Berthier, E., Wagnon, P., Kääh, A., and Treichler, D.: A spatially resolved estimate of High Mountain Asia glacier mass balances from 2000 to 2016, *Nature Geosci*, 10, 668–673, <https://doi.org/10.1038/ngeo2999>, 2017.
- Burns, P. J., Massey, R., and Goetz, S. J.: NASA ABoVE 10m Composite DEM, 2018, G54A-05, 2018.
- 500 Chang, W., Tan, S., Lemmetyinen, J., Tsang, L., Xu, X., and Yueh, S. H.: Dense Media Radiative Transfer Applied to SnowScat and SnowSAR, *IEEE J. Sel. Top. Appl. Earth Observations Remote Sensing*, 7, 3811–3825, <https://doi.org/10.1109/JSTARS.2014.2343519>, 2014.
- Cogley, G. (submitter); Kienholz, C., Miles, E., Sharp, M., and Wyatt, F. (analyst(s)): GLIMS Glacier Database. Boulder, CO. National Snow and Ice Data Center, <http://dx.doi.org/10.7265/N5V98602>, 2015
- 505 Dadic, R., Mott, R., Lehning, M., and Burlando, P.: Wind influence on snow depth distribution and accumulation over glaciers, *Journal of Geophysical Research: Earth Surface*, 115, 2010.
- Davey, C. A., Redmond, K. T., and Simeral, D. B.: Weather and Climate Inventory, National Park Service, ARCN, Natural Resource Technical Report NPS/ARC/NRTR-2007/005, 2007.
- DeVisser, M. H. and Fountain, A. G.: A century of glacier change in the Wind River Range, WY, *Geomorphology*, 232, 103–116, 510 <https://doi.org/10.1016/j.geomorph.2014.10.017>, 2015.
- Dozier, J.: Spectral signature of alpine snow cover from the Landsat Thematic Mapper, *Remote sensing of environment*, 28, 9–22, 1989.
- Evans, S.: Dielectric properties of ice and snow—a review, *Journal of Glaciology*, 5, 773–792, 1965.
- Evison, L. H., Calkin, P. E., and Ellis, J. M.: Late-Holocene glaciation and twentieth-century retreat, northeastern Brooks Range, Alaska, *The Holocene*, 6, 17–24, 1996.
- 515 Fassnacht, S. R. and Deems, J. S.: Scaling associated with averaging and resampling of LIDAR-derived montane snow depth data, in: *Proceedings of the 62nd Eastern Snow Conference*, Waterloo, Ontario, Canada: USA, Eastern Snow Conference, 163–172, 2005.
- Fassnacht, S. R., Sexstone, G. A., Kashipazha, A. H., López-Moreno, J. I., Jasinski, M. F., Kampf, S. K., and Von Thaden, B. C.: Deriving snow-cover depletion curves for different spatial scales from remote sensing and snow telemetry data, *Hydrological Processes*, 30, 1708–1717, <https://doi.org/10.1002/hyp.10730>, 2016.



- 520 Fassnacht, S. R., Patterson, G. G., Venable, N. B. H., Cherry, M. L., Pfohl, A. K. D., Sanow, J. E., and Tedesche, M. E.:
How Do We Define Climate Change? Considering the Temporal Resolution of Niveo-Meteorological Data, *Hydrology*, 7, 38,
<https://doi.org/10.3390/hydrology7030038>, 2020.
- Floricioiu, D. and Rott, H.: Seasonal and short-term variability of multifrequency, polarimetric radar backscatter of Alpine terrain from SIR-
C/X-SAR and AIRSAR data, *IEEE Transactions on Geoscience and Remote Sensing*, 39, 2634–2648, <https://doi.org/10.1109/36.974998>,
525 2001.
- Ganey, G. Q., Loso, M. G., Burgess, A. B., and Dial, R. J.: The role of microbes in snowmelt and radiative forcing on an Alaskan icefield,
Nature Geosci, 10, 754–759, <https://doi.org/10.1038/ngeo3027>, 2017.
- Gardelle, J., Berthier, E., Arnaud, Y., and Kääb, A.: Region-wide glacier mass balances over the Pamir-Karakoram-Himalaya during
1999–2011, *The Cryosphere*, 7, 1263–1286, <https://doi.org/10.5194/tc-7-1263-2013>, 2013.
- 530 GLIMS and NSIDC: Global Land Ice Measurements from Space glacier database. Compiled and made available by the international GLIMS
community and the National Snow and Ice Data Center, Boulder CO, U.S.A. <https://doi.org/10.7265/N5V98602>, 2018.
- Gorelick, N., Hancher, M., Dixon, M., Ilyushchenko, S., Thau, D., and Moore, R.: Google Earth Engine: Planetary-scale geospatial analysis
for everyone, *Remote Sensing of Environment*, 202, 18–27, <https://doi.org/10.1016/j.rse.2017.06.031>, 2017.
- Grünewald, T., Schirmer, M., Mott, R., and Lehning, M.: Spatial and temporal variability of snow depth and ablation rates in a small mountain
535 catchment, *The Cryosphere*, 4, 215–225, <https://doi.org/10.5194/tc-4-215-2010>, 2010.
- Higuchi, K., Iozawa, T., Fujii, Y., and Kodama, H.: Inventory of perennial snow patches in Central Japan, *GeoJournal*, 4,
<https://doi.org/10.1007/BF00219577>, 1980.
- Hirayama, H., Sharma, R. C., Tomita, M., and Hara, K.: Evaluating multiple classifier system for the reduction of salt-and-
pepper noise in the classification of very-high-resolution satellite images, *International Journal of Remote Sensing*, 40, 2542–2557,
540 <https://doi.org/10.1080/01431161.2018.1528400>, 2019.
- Hotaling, S., Foley, M. E., Zeglin, L. H., Finn, D. S., Tronstad, L. M., Giersch, J. J., Muhlfeld, C. C., and Weisrock, D. W.: Microbial assem-
blages reflect environmental heterogeneity in alpine streams, *Global Change Biology*, 25, 2576–2590, <https://doi.org/10.1111/gcb.14683>,
2019.
- Hotaling, S., Lutz, S., Dial, R. J., Anesio, A. M., Benning, L. G., Fountain, A. G., Kelley, J. L., McCutcheon, J., Skiles, S. M., Takeuchi,
545 N., and Hamilton, T. L.: Biological albedo reduction on ice sheets, glaciers, and snowfields, *Earth-Science Reviews*, 220, 103728,
<https://doi.org/10.1016/j.earscirev.2021.103728>, 2021.
- Housman, I. W., Chastain, R. A., and Finco, M. V.: An Evaluation of Forest Health Insect and Disease Survey Data and
Satellite-Based Remote Sensing Forest Change Detection Methods: Case Studies in the United States, *Remote Sensing*, 10, 1184,
<https://doi.org/10.3390/rs10081184>, 2018.
- 550 Irish, R. R., Barker, J. L., Goward, S. N., and Arvidson, T.: Characterization of the Landsat-7 ETM+ automated cloud-cover assessment
(ACCA) algorithm, *Photogrammetric engineering and remote sensing*, 10, 1179–1188, 2006.
- Joly, K.: Modeling influences on winter distribution of caribou in northwestern Alaska through use of satellite telemetry, *Ran*, 75–85,
<https://doi.org/10.7557/2.31.2.1992>, 2011.
- Lehning, M., Löwe, H., Ryser, M., and Raderschall, N.: Inhomogeneous precipitation distribution and snow transport in steep terrain, *Water*
555 *Resources Research*, 44, <https://doi.org/10.1029/2007WR006545>, 2008.
- Lewkowicz, A. G. and Young, K. L.: Hydrology of a Perennial Snowbank in the Continuous Permafrost Zone, Melville Island, Canada,
Geografiska Annaler: Series A, Physical Geography, 72, 13–21, <https://doi.org/10.1080/04353676.1990.11880297>, 1990.



- Li, N., Huo, H., Zhao, Y., Chen, X., and Fang, T.: A Spatial Clustering Method With Edge Weighting for Image Segmentation, *IEEE Geoscience and Remote Sensing Letters*, 10, 1124–1128, <https://doi.org/10.1109/LGRS.2012.2231662>, 2013.
- 560 Liang, D., Guo, H., Zhang, L., Cheng, Y., Zhu, Q., and Liu, X.: Time-series snowmelt detection over the Antarctic using Sentinel-1 SAR images on Google Earth Engine, *Remote Sensing of Environment*, 256, 112318, <https://doi.org/10.1016/j.rse.2021.112318>, 2021.
- Lievens, H., Brangers, I., Marshall, H.-P., Jonas, T., Olefs, M., and De Lannoy, G.: Sentinel-1 snow depth retrieval at sub-kilometer resolution over the European Alps, *Snow/Remote Sensing*, <https://doi.org/10.5194/tc-2021-74>, 2021.
- Lievens, H., Demuzere, M., Marshall, H.-P., Reichle, R. H., Brucker, L., Brangers, I., de Rosnay, P., Dumont, M., Giroto, M., Immerzeel, W.
565 W., Jonas, T., Kim, E. J., Koch, I., Marty, C., Saloranta, T., Schöber, J., and De Lannoy, G. J. M.: Snow depth variability in the Northern Hemisphere mountains observed from space, *Nat Commun*, 10, 4629, <https://doi.org/10.1038/s41467-019-12566-y>, 2019.
- Luetschg, M., Stoeckli, V., Lehning, M., Haeberli, W., and Ammann, W.: Temperatures in two boreholes at Flüela Pass, Eastern Swiss Alps: the effect of snow redistribution on permafrost distribution patterns in high mountain areas, *Permafrost and Periglacial Processes*, 15, 283–297, <https://doi.org/10.1002/ppp.500>, 2004.
- 570 Lv, Z., Liu, T., and Benediktsson, J. A.: Object-Oriented Key Point Vector Distance for Binary Land Cover Change Detection Using VHR Remote Sensing Images, *IEEE Transactions on Geoscience and Remote Sensing*, 58, 6524–6533, <https://doi.org/10.1109/TGRS.2020.2977248>, 2020.
- Macander, M. J., Swingley, C. S., Joly, K., and Reynolds, M. K.: Landsat-based snow persistence map for northwest Alaska, *Remote Sensing of Environment*, 163, 23–31, <https://doi.org/10.1016/j.rse.2015.02.028>, 2015.
- 575 Mätzler, C.: Applications of the interaction of microwaves with the natural snow cover, *Remote Sensing Reviews*, 2, 259–387, <https://doi.org/10.1080/02757258709532086>, 1987.
- McHugh, M. L.: Interrater reliability: the kappa statistic, *Biochemia Medica*, 22, 276–282, 2012.
- Muller, F.: Inventory of glaciers in the Mount Everest region, *Perennial ice and snow masses*, 47–53, 1970.
- Mülmenstädt, J., Lubin, D., Russell, L. M., and Vogelmann, A. M.: Cloud Properties over the North Slope of Alaska: Identifying the
580 Prevailing Meteorological Regimes, *Journal of Climate*, 25, 8238–8258, <https://doi.org/10.1175/JCLI-D-11-00636.1>, 2012.
- Naegeli, K., Damm, A., Huss, M., Wulf, H., Schaepman, M., and Hoelzle, M.: Cross-Comparison of Albedo Products for Glacier Surfaces Derived from Airborne and Satellite (Sentinel-2 and Landsat 8) Optical Data, *Remote Sensing*, 9, 110, <https://doi.org/10.3390/rs9020110>, 2017.
- Nagler, T., Rott, H., Ripper, E., Bippus, G., and Hetzenecker, M.: Advancements for Snowmelt Monitoring by Means of Sentinel-1 SAR,
585 *Remote Sensing*, 8, 348, <https://doi.org/10.3390/rs8040348>, 2016.
- Paul, F., Winsvold, S., Kääb, A., Nagler, T., and Schwaizer, G.: Glacier Remote Sensing Using Sentinel-2. Part II: Mapping Glacier Extents and Surface Facies, and Comparison to Landsat 8, *Remote Sensing*, 8, 575, <https://doi.org/10.3390/rs8070575>, 2016.
- Poortinga, A., Tenneson, K., Shapiro, A., Nquyen, Q., San Aung, K., Chishtie, F., and Saah, D.: Mapping Plantations in Myanmar by Fusing Landsat-8, Sentinel-2 and Sentinel-1 Data along with Systematic Error Quantification, *Remote Sensing*, 11, 831,
590 <https://doi.org/10.3390/rs11070831>, 2019.
- Potin, M. P., Rosich, M. B., Grimont, M. P., Miranda, M. N., Shurmer, M. I., O’Connell, M. A., Torres, M. R., and Krassenburg, M. M.: Sentinel-1 Mission Status, 6, 2016.
- Rattenbury, K., Kielland, K., Finstad, G., and Schneider, W.: A reindeer herder’s perspective on caribou, weather and socio-economic change on the Seward Peninsula, Alaska, *Polar Research*, 28, 71–88, <https://doi.org/10.1111/j.1751-8369.2009.00102.x>, 2009.



- 595 Reber, B., Mätzler, C., and Schanda, E.: Microwave signatures of snow crusts Modelling and measurements, *International Journal of Remote Sensing*, 8, 1649–1665, <https://doi.org/10.1080/01431168708954805>, 1987.
- Rosvold, J.: Perennial ice and snow-covered land as important ecosystems for birds and mammals, *Journal of Biogeography*, 43, 3–12, <https://doi.org/10.1111/jbi.12609>, 2016.
- Rott, H. and Mätzler, C.: Possibilities and Limits of Synthetic Aperture Radar for Snow and Glacier Surveying, *Annals of Glaciology*, 9, 195–199, <https://doi.org/10.3189/S0260305500000604>, 1987.
- 600 Roy, D. P., Li, J., Zhang, H. K., Yan, L., Huang, H., and Li, Z.: Examination of Sentinel-2A multi-spectral instrument (MSI) reflectance anisotropy and the suitability of a general method to normalize MSI reflectance to nadir BRDF adjusted reflectance, *Remote Sensing of Environment*, 199, 25–38, <https://doi.org/10.1016/j.rse.2017.06.019>, 2017.
- Schwerdt, M., Schmidt, K., Tous Ramon, N., Klenk, P., Yague-Martinez, N., Prats-Iraola, P., Zink, M., and Geudtner, D.: Independent System Calibration of Sentinel-1B, *Remote Sensing*, 9, 511, <https://doi.org/10.3390/rs9060511>, 2017.
- 605 Shi, J. and Dozier, J.: Inferring snow wetness using C-band data from SIR-C's polarimetric synthetic aperture radar, *IEEE Transactions on Geoscience and Remote Sensing*, 33, 905–914, <https://doi.org/10.1109/36.406676>, 1995.
- Small, D.: Flattening Gamma: Radiometric Terrain Correction for SAR Imagery, *IEEE Trans. Geosci. Remote Sensing*, 49, 3081–3093, <https://doi.org/10.1109/TGRS.2011.2120616>, 2011.
- 610 Stillinger, T., Roberts, D. A., Collar, N. M., and Dozier, J.: Cloud Masking for Landsat 8 and MODIS Terra Over Snow-Covered Terrain: Error Analysis and Spectral Similarity Between Snow and Cloud, *Water Resour. Res.*, 55, 6169–6184, <https://doi.org/10.1029/2019WR024932>, 2019.
- Strozzi, T., Wiesmann, A., and Mätzler, C.: Active microwave signatures of snow covers at 5.3 and 35 GHz, *Radio Science*, 32, 479–495, <https://doi.org/10.1029/96RS03777>, 1997.
- 615 Tedesche, M. E., Fassnacht, S. R., and Meiman, P. J.: Scales of snow depth variability in high elevation rangeland sagebrush, *Front. Earth Sci.*, 11, 469–481, <https://doi.org/10.1007/s11707-017-0662-z>, 2017.
- Tedesche, M. E., Trochim, E. D., Fassnacht, S. R., and Wolken, G. J.: Extent Changes in the Perennial Snowfields of Gates of the Arctic National Park and Preserve, Alaska, *Hydrology*, 6, 53, <https://doi.org/10.3390/hydrology6020053>, 2019.
- Tiuri, M., Sihvola, A., Nyfors, E., and Hallikaiken, M.: The complex dielectric constant of snow at microwave frequencies, *IEEE J. Oceanic Eng.*, 9, 377–382, <https://doi.org/10.1109/JOE.1984.1145645>, 1984.
- 620 Toupin, B., Huot, J., and Manseau, M.: Effect of Insect Harassment on the Behaviour of the Rivière George Caribou, *Arctic*, 49, 375–382, 1996.
- Ulaby, F.T., Long, D.G., Blackwell, W.J., Elachi, C., Fung, A.K., Ruf, C., Sarabandi, K., Zebker, H.A. and Van Zyl, J.: Microwave radar and radiometric remote sensing, *Ann Arbor: University of Michigan Press*, 4, 6, 2014.
- 625 Vieira, S. M., Kaymak, U., and Sousa, J. M. C.: Cohen's kappa coefficient as a performance measure for feature selection, in: *International Conference on Fuzzy Systems*, International Conference on Fuzzy Systems, 1–8, <https://doi.org/10.1109/FUZZY.2010.5584447>, 2010.
- Vollrath, A., Mullissa, A., and Reiche, J.: Angular-Based Radiometric Slope Correction for Sentinel-1 on Google Earth Engine, *Remote Sensing*, 12, 1867, <https://doi.org/10.3390/rs12111867>, 2020.
- Winfree, R.: Climate change scenario planning for interior arctic Alaska parks: Noatak–Gates of the Arctic–Kobuk Valley, *US Department of the Interior, National Park Service, Natural Resource Stewardship and Science*, 2014.
- 630 Wolken, G. J., England, J. H., and Dyke, A. S.: Re-Evaluating the Relevance of Vegetation Trimlines in the Canadian Arctic as an Indicator of Little Ice Age Paleoenvironments, *Arctic*, 58, 341–353, 2005.



- Yoshikawa, K., Hinzman, L. D., and Kane, D. L.: Spring and aufeis (icing) hydrology in Brooks Range, Alaska, *Journal of Geophysical Research: Biogeosciences*, 112, <https://doi.org/10.1029/2006JG000294>, 2007.
- 635 Zhang, T., Osterkamp, T. E., and Stamnes, K.: Some Characteristics of the Climate in Northern Alaska, U.S.A., *Arctic and Alpine Research*, 28, 509, <https://doi.org/10.2307/1551862>, 1996.
- Zhu, Z. and Woodcock, C. E.: Object-based cloud and cloud shadow detection in Landsat imagery, *Remote Sensing of Environment*, 118, 83–94, <https://doi.org/10.1016/j.rse.2011.10.028>, 2012.
- Zhu, Z., Wang, S., and Woodcock, C. E.: Improvement and expansion of the Fmask algorithm: cloud, cloud shadow, and snow detection for
640 Landsats 4–7, 8, and Sentinel 2 images, *Remote Sensing of Environment*, 159, 269–277, <https://doi.org/10.1016/j.rse.2014.12.014>, 2015.